Micromechanical model for off-axis creep rupture in unidirectional composites undergoing finite strains

Kovačević, Dragan; Sundararajan, Bharath K.; van der Meer, Frans P.

DOI
10.1016/j.compositesa.2023.107860

Publication date
2023

Document Version
Final published version

Published in
Composites Part A: Applied Science and Manufacturing

Citation (APA)
Kovačević, D., Sundararajan, B. K., & van der Meer, F. P. (2023). Micromechanical model for off-axis creep rupture in unidirectional composites undergoing finite strains. *Composites Part A: Applied Science and Manufacturing*, *176*, Article 107860. https://doi.org/10.1016/j.compositesa.2023.107860

Composites: Part A 176 (2024) 107860

Contents lists available at ScienceDirect

Composites Part A

journal homepage: www.elsevier.com/locate/compositesa

Book reviews

Micromechanical model for off-axis creep rupture in unidirectional composites undergoing finite strains

Dragan Kovačević [a,c,*], Bharath K. Sundararajan [b,c], Frans P. van der Meer [a]

[a] Delft University of Technology, Faculty of Civil Engineering and Geosciences, PO Box 5048, 2600 GA Delft, The Netherlands
[b] University of Twente, Faculty of Engineering Technology, PO Box 217, 7522 LW, Enschede, The Netherlands
[c] Dutch Polymer Institute (DPI), PO Box 902, 5600 AX, Eindhoven, The Netherlands

ARTICLE INFO

Dataset link: http://dx.doi.org/10.4121/21835773.v1

Keywords:
Thermoplastic composites
Cohesive zone modeling
Energy-based initiation
Homogenization

ABSTRACT

A microscale numerical framework for modeling creep rupture in unidirectional composites under off-axis loading is presented, building on recent work on imposing off-axis loading on a representative volume element. Creep deformation of the thermoplastic polymer matrix is accounted for by means of the Eindhoven Glassy Polymer material model. Creep rupture is represented with cohesive cracks, combining an energy-based initiation criterion with a time-dependent cohesive law and a global failure criterion based on the minimum in homogenized creep strain-rate. The model is compared against experiments on carbon/PEEK composite material tested at different off-axis angles, stress levels and temperatures. Creep deformation is accurately reproduced by the model, except for small off-axis angles, where the observed difference is ascribed to macroscopic variations in the experiment. Trends in rupture time are also reproduced although quantitative rupture time predictions are not for all test cases accurate.

1. Introduction

Structural parts made of fiber reinforced polymer (FRP) composites usually require operational time that spans from several years to several decades [1]. Therefore, the long-term structural integrity of these components is of utmost importance. A challenge to this requirement is the inherent time dependent mechanical response of the composites which has its roots in the viscous nature of the polymer matrix. When exposed to a constant stress level FRP composites will undergo creep deformation, whose magnitude further depends on the off-axis loading angle, temperature, moisture, etc.

Many models that describe deformation kinetics of polymers are based on the Eyring thermally activated flow theory [2]. Kanters et al. [3] represented a constant plastic strain-rate in thermoplastic polymers and composites and applied a creep rupture criterion based on a critical value of the plastic strain accumulated in the material. The similar idea was followed by Erartsin et al. [4] and extended to off-axis failure of unidirectional (UD) glass/iPP composite systems. Also based on the Eyring flow theory, Spathis and Kontou [5] proposed an equation for the creep strain-rate, and assumed the creep rupture time as the moment when the creep strain-rate reaches a minimum value. Raghavan and Meshii [6] developed a creep rupture model for composites, in which the creep strain is modeled by the thermal activation theory, and the creep rupture happens when the stored elastic energy in the material attains a critical value. As an alternative to the Eyring flow theory, the single integral approach developed by Schapery [7] has often been used to represent the creep behavior in polymers. Lou and Schapery [8] showed that this theory can also represent the creep response of composites for different stress levels and off-axis angles. All models for the composite material mentioned so far aim to describe the homogenized response in (semi-)analytical form. Although this approach is computationally efficient, complete characterization of the homogenized orthotropic material is challenging, giving rise to complex formulations and extensive experimental identification procedures.

On the other side, computationally more expensive microscale models explicitly account for the heterogeneous microstructure of the composite material. In this context a numerical implementation of the Schapery's model for polymers was done by Haj-Ali and Muliana [9], and later used in the Aboudi four-cell micromodel [10] to represent the creep response of different FRP composites under off-axis loading [11], but no creep rupture was predicted. Jafaripour and Taheri-Behrooz [12] also applied the Schapery's integral to model creep behavior in a UD composite representative volume element (RVE). However, the RVE model is not suitable for every fiber orientation and does not predict creep rupture. In order to represent degradation

* Corresponding author at: Delft University of Technology, Faculty of Civil Engineering and Geosciences, PO Box 5048, 2600 GA Delft, The Netherlands.
E-mail addresses: d.kovacevic-1@tudelft.nl (D. Kovačević), b.k.sundararajan@utwente.nl (B.K. Sundararajan), f.p.vandermeer@tudelft.nl (F.P. van der Meer).

https://doi.org/10.1016/j.compositesa.2023.107860
Received 20 February 2023; Received in revised form 1 October 2023; Accepted 18 October 2023
Available online 7 November 2023

of the composite constituents on the microlevel, Gal and Fish [13] applied an isotropic continuum creep damage model [14,15], followed by the upscaling of the unit cell response in structural analyses of composite components. In a multiscale model aimed at predicting the time-dependent response of UD composites Govaert et al. [16] also addressed creep failure due to off-axis loading. The model assumes a regular distribution of fibers in the RVE, and a failure criterion based on the critical plastic strain at one point in the RVE.

Despite the vast amount of literature dealing with the micromechanical modeling of FRP composites, only a small part concerns the creep behavior and to our knowledge only the model by Gal and Fish [13] describes progressive creep rupture of the material. Recently, we have developed a micromechanical model to impose a constant strain-rate on the RVE under an off-axis angle [17], assuming finite deformations in the material locally and in the homogenized sense. The model was supplemented with a cohesive surface methodology to simulate rate-dependent failure in thermoplastic composites [18]. In this study the microscale numerical model is modified to apply a constant stress on the RVE and analyze off-axis creep rupture in unidirectional composites. The Eindhoven Glassy Polymer (EGP) material model is used to represent the creep behavior in the polymer matrix. In order to simulate the rupture process, a modified version of the Reiner–Weissenberg material failure theory [19] is proposed. Specifically, when the Helmholtz free energy of the EGP model locally reaches a critical value, a cohesive segment is inserted in the RVE. The necessity to use a time-dependent cohesive law to model decohesion due to creep loading is illustrated. Global failure of the material coincides with the homogenized creep strain-rate of the RVE reaching a minimum value. Simulation results obtained for different off-axis angles, temperatures and stress levels are compared with experimental observations on a UD carbon/polyetheretherketone (PEEK) composite system.

The paper is organized as follows: the experimental benchmark for comparing the model predictions is introduced in the next section. Then the micromechanical framework is outlined, with emphasis on the changes with respect to earlier work [17,18]. In the subsequent section the constitutive models for the composite constituents are explained. Afterward, the results obtained by the model are compared with experiments.

2. Experimental benchmark

Carbon fiber reinforced UD tapes with PEEK matrix were provided by Solvay. Previous research efforts by Erartsin et al. [20] on commercial UD tapes with the fiber volume fraction V_f of 0.6, showed a large scatter in the experimental data. Hence in this study tapes with more matrix ($V_f = 0.4$) than commercial tapes were preferred to ensure good repeatability of data. The tensile test coupons were prepared according to the procedure outlined in [18]. The coupons had a thickness of 1.8 mm and a width of 15 mm. A gauge length of 100 mm was used for 90° and 45° loaded samples. For smaller loading angles of 30° and 15°, a longer gauge length of 120 mm was used to contain the failure within the gauge section. A tab length of 25 mm was utilized to carry out the experiments. However, while carrying out experiments at higher temperature, smaller clamps that could fit inside the temperature chamber were used, with a reduced tab length of 20 mm.

Creep experiments under uniaxial tension at room temperature were performed using a Zwick Z100 universal tensile tester equipped with a 50 kN load cell. Zwick Z05 tester equipped with a smaller 5 kN load cell was used for higher temperature experiments, also utilizing temperature chambers with digital controls to ensure precise control of temperature, see Fig. 1(right). A constant force was applied on the specimen, from which the engineering (eng.) stress was computed. The reported creep strains are a direct translation of the crosshead displacement, and measure the engineering strain. A schematic representation of the testing specimen is shown in Fig. 1(left), where χ is the initial angle between the fibers and loading direction, often referred to as the off-axis angle. It is defined as $\chi = 90° - \theta_0$, where θ_0 is the initial angle between the global x-axis and the fibers, see Fig. 2.

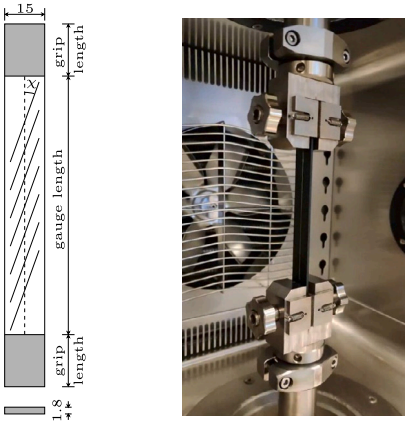

Fig. 1. Schematic representation of testing specimen (left), where χ is the initial off-axis angle; creep testing of UD carbon/PEEK composite system at higher temperature in a temperature chamber (right); dimensions in mm.

3. Micromechanical framework

3.1. Homogenized kinematics and external force vector

In this section, the equations needed to impose a constant Cauchy stress on the RVE under an off-axis angle and compute the logarithmic strain in the global loading direction are presented. To facilitate the comparison with experimental results, the adjustment to impose a constant engineering stress on the RVE and calculate the engineering strain is introduced afterward.

In the case at hand unidirectional composite material is exposed to a constant stress, i.e., to creep loading conditions, see Fig. 2(left). Beside the extensional deformation, this uniaxial loading will deform the orthotropic material also in shear, see Fig. 2(middle). Due to the viscous nature of the polymer matrix, deformation in the material will keep increasing. Furthermore, accounting for finite strains in the material the local coordinate frame aligned with the reinforcement may change orientation from the angle θ_0 to a new angle θ_1. Given the angle θ_1 the stress state can be transformed to the local coordinate frame, resulting in the Cauchy stress components shown in Fig. 2(right). We aim to simulate this deformation process on the microscale, by means of an RVE model of a thin slice of material perpendicular to the fibers. Therefore, the homogenized stress components acting on the RVE, see Fig. 3(left), must be equal to the stress components in Fig. 2(right). This condition implies that the RVE, which is defined in the local coordinate system aligned with the fibers, must account for the change in orientation during the deformation process from the angle θ_0 to the angle θ_1. To satisfy this requirement, proper kinematic relations and the external force vector components acting on the micromodel need to be derived for a thin slice RVE. Defining an off-axis uniaxial stress state in an RVE while accounting for a possible update in its orientation can be achieved with the arclength formulation proposed in [17]. This formulation was originally designed for constant strain-rate simulations, where the deformation in load direction is known for every time step while the magnitude of the stress is not. By contrast, for creep simulations, the stress magnitude is given and the corresponding deformation unknown, which asks for a small modification of the formulation. We consider an RVE with periodic boundary conditions [21], that also enforce the periodicity in microcracking [22]. Homogenized kinematic relations are defined following displacement components of master nodes of the RVE. Active displacements of the master nodes are shown in Fig. 3(right), accompanied with non-zero force components. Master node displacements not indicated in the figure are set to zero. The detailed discussion of this choice of boundary conditions is presented in [17].

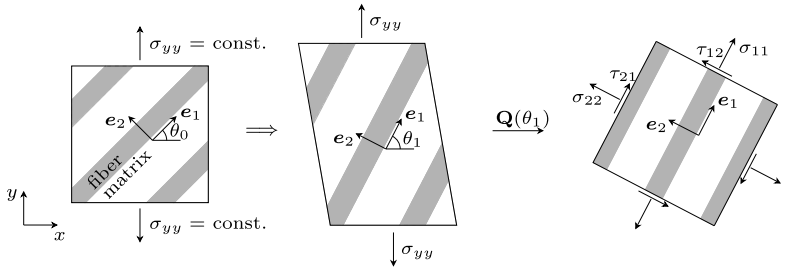

Fig. 2. Constant stress applied on unidirectional composite material (left); deformed material due to uniaxial loading (middle); Cauchy stresses in local coordinate system (right).

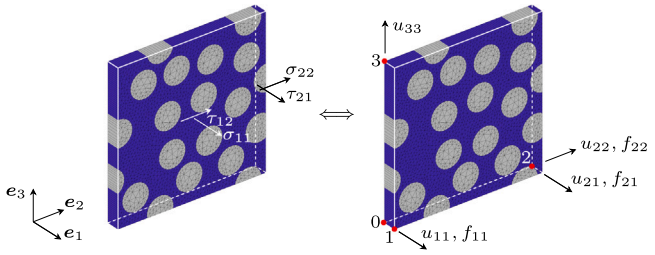

Fig. 3. Homogenized stress components on RVE faces (left) as result of force components applied on RVE master nodes (right); non-zero displacement components of four RVE master nodes also indicated in the right figure.

To derive expressions for the external force components, first we need to introduce the homogenized deformation gradient of the RVE, $\bar{\mathbf{F}}$. With the Dirichlet boundary conditions as defined in Fig. 3(right), the homogenized deformation gradient is:

$$\bar{\mathbf{F}} = \begin{bmatrix} \bar{F}_{11} & \bar{F}_{12} & 0 \\ 0 & \bar{F}_{22} & 0 \\ 0 & 0 & \bar{F}_{33} \end{bmatrix} = \begin{bmatrix} 1 + \frac{u_{11}}{l_1^0} & \frac{u_{21}}{l_2^0} & 0 \\ 0 & 1 + \frac{u_{22}}{l_2^0} & 0 \\ 0 & 0 & 1 + \frac{u_{33}}{l_3^0} \end{bmatrix} \tag{1}$$

where u_{ij} is displacement of master node i in direction j, and l_i^0 is the initial length of the RVE in direction i. Components of the external force vector are derived considering the equilibrium between the homogenized internal and external force vector: $\bar{\mathbf{f}}^{\text{int}} = \bar{\mathbf{f}}^{\text{ext}}$. Without loss of generality we assume that the whole RVE domain is represented with a single trilinear hexahedral finite element. Following Belytchko et al. [23] the homogenized internal force vector can be expressed as:

$$\bar{\mathbf{f}}^{\text{int}} = \int_{\Omega_0} \bar{\mathbf{B}}_0^{\mathrm{T}} \bar{\mathbf{F}}^{-1} \bar{\boldsymbol{\sigma}} \bar{J} d\Omega_0 \tag{2}$$

in which $\bar{\mathbf{B}}_0$ is the strain — nodal displacement matrix defined over the reference configuration, $\bar{J}$ is the determinant of $\bar{\mathbf{F}}$, while $\bar{\boldsymbol{\sigma}}$ represents the homogenized Cauchy stress acting on the material in the local frame. After evaluating the integral in Eq. (2), the expressions for the corresponding external force vector components acting on the master nodes yield:

$$\begin{aligned} f_{11} &= \sigma_{yy} A_1^0 \bar{J} \left(\frac{s_1^2}{\bar{F}_{11}} - c_1 s_1 \frac{\bar{F}_{12}}{\bar{F}_{11}\bar{F}_{22}} \right) \\ f_{21} &= \sigma_{yy} A_2^0 \bar{J} \frac{c_1 s_1}{\bar{F}_{22}} \\ f_{22} &= \sigma_{yy} A_2^0 \bar{J} \frac{c_1^2}{\bar{F}_{22}} \end{aligned} \tag{3}$$

Here f_{ij} is force component acting on master node i in direction j, A_i^0 is the initial surface of the RVE on which a corresponding stress component is acting, while s_i and c_i denote $\sin(\theta_i)$ and $\cos(\theta_i)$ respectively, with i being either 0 or 1. The angle θ_1 is computed as: $\theta_1 = \theta_0 + \phi$, where the angle ϕ represents the change in orientation of the RVE in the deformation process. Following [17], it can be expressed as:

$$\phi = \arctan\left(\frac{-\bar{F}_{11} c_0 s_0 + \bar{F}_{12} s_0^2 + \bar{F}_{22} c_0 s_0}{\bar{F}_{11} c_0^2 - \bar{F}_{12} c_0 s_0 + \bar{F}_{22} s_0^2} \right) \tag{4}$$

The expressions for the force components, Eq. (3), are very similar to the unit force components of the strain-rate based arclength model [17], differing only for the presence of the creep stress σ_{yy}. When periodic boundary conditions are applied, every force component in Eq. (3) is distributed over the nodes belonging to the side of the RVE on which the force component is acting. This way, the external force vector $\mathbf{f}^{\text{ext}}$ applied on the RVE is fully defined. This vector has to be in equilibrium with the internal force vector, i.e., $\mathbf{f}^{\text{ext}} = \mathbf{f}^{\text{int}}$. In the presence of cracks, and the absence of body forces, the internal force vector is defined as presented in [18].

Since we are dealing with the creep problem, it is pertinent to plot the strain in the material versus time. For this purpose an expression for the homogenized strain component ε_{yy} corresponding to the creep stress in the global loading direction needs to be derived. To find this expression, a relation between the RVE homogenized deformation gradient and the deformation gradient $\mathbf{F}$ of the material in the global frame is needed. Due to the analogy between an off-axis creep stress and an off-axis strain-rate loading, we can follow the transformation rules and kinematic relations derived in [17] for an off-axis strain-rate acting on the material. Accordingly:

$$\mathbf{F} = \mathbf{Q}_1^{\mathrm{T}} \bar{\mathbf{F}} \mathbf{Q}_0 \tag{5}$$

In this equation $\mathbf{Q}_0$ is the transformation matrix that depends on the angle θ_0:

$$\mathbf{Q}_0 = \begin{bmatrix} \cos(\theta_0) & \sin(\theta_0) & 0 \\ -\sin(\theta_0) & \cos(\theta_0) & 0 \\ 0 & 0 & 1 \end{bmatrix} \tag{6}$$

The transformation matrix $\mathbf{Q}_1$ has the same form, although it depends on the angle θ_1. Given Eq. (5), the homogenized strain in the loading direction can be written as:

$$\varepsilon_{yy} = \ln(F_{yy}) \tag{7}$$

where F_{yy} is the component of $\mathbf{F}$ in the global loading direction.

Eqs. (3) and (7), impose the homogenized Cauchy (true) stress on the RVE and measure the homogenized logarithmic (true) strain, respectively. However, the experimental results are reported in the form of engineering strain as the result of a constant force imposed on the specimen. The consequence of applying the constant force and relying on the engineering stress, is that the actual stress on the material changes with deformation. In that regard, the Cauchy stress σ_{yy} in Eq. (3) is computed from the engineering stress σ_{yy}^{eng}:

$$\sigma_{yy} = \frac{\sigma_{yy}^{\text{eng}}}{F_{xx} F_{zz}} \tag{8}$$

where F_{xx} and F_{zz} are components of the homogenized deformation gradient in the global frame, Eq. (5). Finally, the engineering strain in the global loading direction is extracted from the model as follows:

$$\varepsilon_{yy}^{\text{eng}} = F_{yy} - 1 \tag{9}$$

Table 1
Algorithm of the microscale creep model for time step n.

(1) set step size Δt
(2) given $\bar{\mathbf{F}}^{n-1}$, compute ϕ from Eq. (4); set $\theta_1 = \theta_0 + \phi$
(3) update $\mathbf{f}^{\text{ext}}$ using Eqs. (3) and (10), for eng. stress–strain use Eq. (8) in Eq. (3)
(4) follow the algorithm outlined in [24]
(5) if commit, compute ε_{yy} combining Eqs. (5) and (7),
for eng. strain, compute $\varepsilon_{yy}^{\text{eng}}$ combining Eqs. (5) and (9)

3.2. Implementation

The computational framework for the model presented herein is based on the updated Lagrangian formulation [23], an approach suitable for modeling finite deformations. The equations introduced so far assume no discretization in time. However, in the spirit of a force controlled analysis an incremental-iterative procedure is applied, with a finite time increment Δt in every simulation step. In order to match the experiment in terms of the time needed to reach a constant load level, the engineering stress-rate $\dot{\sigma}_{yy}^{\text{eng}}$ is considered, such that at time step n the engineering stress in Eq. (8) is computed as follows:

$$\sigma_{yy,n}^{\text{eng}} = \min\left(\sigma_{yy,n-1}^{\text{eng}} + \dot{\sigma}_{yy}^{\text{eng}}\Delta t, \sigma_{yy}^{\text{const}}\right) \tag{10}$$

where $\sigma_{yy}^{\text{const}}$ is the constant (engineering) stress. If the simulation considers a constant Cauchy stress, then the superscript "eng" is dropped from Eq. (10) and $\sigma_{yy,n}$ is directly applied in Eq. (3) without correcting the stress for the previous deformation, as done in Eq. (8) for the engineering stress. The algorithm for one time step of the analysis is presented in Table 1. The core part of the implementation with adaptive stepping and insertion of cohesive cracks on the fly coincides with the algorithm introduced by Van der Meer and Sluys [24]. It should be noted that the external force vector is computed knowing the homogenized deformation gradient from the last converged time step $\bar{\mathbf{F}}^{n-1}$, and no update in the $\mathbf{f}^{\text{ext}}$ is made during iterations within the current time step.

4. Constitutive models

In this section the constitutive models representing the behavior of the composite constituents are outlined. The description of the EGP model for the polymer matrix is followed by explaining a transversely isotropic material model for carbon fibers. The creep rupture process is simulated with interelement cohesive surfaces that are inserted during the simulation. For the creep simulations, a new cohesive zone (CZ) initiation criterion is proposed as well as a time-dependent cohesive law.

4.1. The Eindhoven Glassy Polymer constitutive model

To represent the behavior of the polymer matrix we choose the EGP material model. The EGP is a 3D elasto-viscoplastic model without a yield surface. Instead, it is based on the Eyring flow theory [2], in the sense that the viscosity reduces with the stress applied on the material [25], leading to the flow of the polymer. In this regard, the yield point is perceived as the stress induced melting [26].

The model formulation builds upon the multiplicative decomposition of the deformation gradient in the elastic and the plastic part:

$$\mathbf{F}_i = \mathbf{F}_{ie} \cdot \mathbf{F}_{ip} \tag{11}$$

To make the distinction from the homogenized deformation gradient of the RVE in the global frame, Eq. (5), the subscript i is used to indicate the deformation gradient at integration point i inside the RVE. It is assumed that the plastic part of deformation is volume preserving, such that:

$$J_i = \det(\mathbf{F}_i) = \det(\mathbf{F}_{ie}) \tag{12}$$

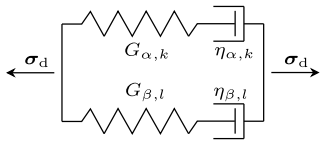

Fig. 4. Mechanical analog for multi-process, multi-mode driving stress in the EGP model.

The derivation of the Cauchy stress follows from principles of continuum thermodynamics as described by Khaleghi et al. [27], but without damage. Following the Clausius–Duhem inequality, the internal dissipation for an isothermal process can be written as:

$$\mathcal{D}_{\text{int}} = \boldsymbol{\sigma} : \mathbf{L} - \frac{1}{J_i}\dot{\psi} \geq 0 \tag{13}$$

where $\boldsymbol{\sigma}$ is the Cauchy stress, $\mathbf{L}$ is the velocity gradient, and ψ is the Helmholtz free energy. The free energy is decomposed in the hydrostatic part ψ_{h}, the hardening part ψ_{r}, and the driving part ψ_{d}. The definition of the hydrostatic free energy is the same as in [27]:

$$\psi_{\text{h}} = \frac{\kappa}{2}(J_i - 1)^2 \tag{14}$$

in which κ is the bulk modulus. The hardening part of the free energy is different than in [27] and is defined such that the derived stress component corresponds to the neo-Hookean model [26]. Accordingly:

$$\psi_{\text{r}} = \frac{G_{\text{r}}}{2}\left[\text{tr}\left(\tilde{\mathbf{B}}\right) - 3\right] \tag{15}$$

where G_{r} is the hardening modulus, and $\tilde{\mathbf{B}}$ is the isochoric left Cauchy–Green deformation tensor:

$$\tilde{\mathbf{B}} = J_i^{-2/3}\left(\mathbf{F}_i \cdot \mathbf{F}_i^{\text{T}}\right) \tag{16}$$

The driving component allows for thermorheologically complex response of the model, meaning that multiple relaxation processes may govern the material response. In this study, we consider two relaxation processes, α and β. In addition to this, each relaxation process may be represented by a number of Maxwell elements connected in parallel, with the mechanical analog of the stress tensor corresponding to the driving free energy shown in Fig. 4. Therefore, the driving free energy is defined as:

$$\psi_{\text{d}} = \frac{1}{2}\sum_{k=1}^{p} G_{\alpha,k}\left[\text{tr}\left(\tilde{\mathbf{B}}_{\text{e}\alpha,k}\right) - 3\right] + \frac{1}{2}\sum_{l=1}^{q} G_{\beta,l}\left[\text{tr}\left(\tilde{\mathbf{B}}_{\text{e}\beta,l}\right) - 3\right] \tag{17}$$

In this equation, p and q are the number of modes respectively for process α and β, $G_{x,j}$ is the shear modulus of Maxwell element j belonging to relaxation process x, where x is either α or β, and j is either k or l, $\tilde{\mathbf{B}}_{\text{e}x,j}$ is the isochoric elastic left Cauchy–Green deformation tensor of the same Maxwell element.

Given the definition of the free energy, the corresponding stress tensors can be defined. Following the Coleman–Noll formalism [28] and the procedure outlined in [27] the stress tensors corresponding to the free energy components emerge as:

$$\begin{aligned}
\boldsymbol{\sigma}_{\text{h}} &= \kappa(J_i - 1)\mathbf{I} \\
\boldsymbol{\sigma}_{\text{r}} &= \frac{1}{J_i}G_{\text{r}}\tilde{\mathbf{B}}^{\text{d}} \\
\boldsymbol{\sigma}_{\text{d}} &= \sum_{k=1}^{p}\boldsymbol{\sigma}_{\alpha,k} + \sum_{l=1}^{q}\boldsymbol{\sigma}_{\beta,l} \\
&= \frac{1}{J_i}\sum_{k=1}^{p} G_{\alpha,k}\tilde{\mathbf{B}}_{\text{e}\alpha,k}^{\text{d}} + \frac{1}{J_i}\sum_{l=1}^{q} G_{\beta,l}\tilde{\mathbf{B}}_{\text{e}\beta,l}^{\text{d}}
\end{aligned} \tag{18}$$

where $\mathbf{I}$ is the second-order unit tensor, and the total Cauchy stress is the summation of three stress tensors, the hydrostatic stress $\boldsymbol{\sigma}_{\text{h}}$, the hardening stress $\boldsymbol{\sigma}_{\text{r}}$, and the driving stress $\boldsymbol{\sigma}_{\text{d}}$: $\boldsymbol{\sigma} = \boldsymbol{\sigma}_{\text{h}} + \boldsymbol{\sigma}_{\text{r}} + \boldsymbol{\sigma}_{\text{d}}$.

Table 2
EGP model parameters.

κ [MPa]	G_r [MPa]	V_α [nm^3]	V_β [nm^3]	ΔH_α [kJ/mol]	ΔH_β [kJ/mol]	$\mu_\alpha = \mu_\beta$	$S_\alpha = S_\beta$
2600	25	3.518	3.518	375.87	325.28	0.08	0

In order to determine $\tilde{\mathbf{B}}^{\mathrm{d}}_{\mathrm{ex},j}$ in Eq. (18) it is necessary to integrate the rate equation of $\tilde{\mathbf{B}}_{\mathrm{ex},j}$:

$$\dot{\tilde{\mathbf{B}}}_{\mathrm{ex},j} = \left(\tilde{\mathbf{L}} - \mathbf{D}_{\mathrm{px},j}\right) \cdot \tilde{\mathbf{B}}_{\mathrm{ex},j} + \tilde{\mathbf{B}}_{\mathrm{ex},j} \cdot \left(\tilde{\mathbf{L}}^{\mathrm{T}} - \mathbf{D}_{\mathrm{px},j}\right) \tag{19}$$

Here, $\mathbf{D}_{\mathrm{px},j}$ is the plastic part of the rate of deformation tensor of Maxwell element j as part of relaxation process x, which is defined by introducing a constitutive relation of the form [29]:

$$\mathbf{D}_{\mathrm{px},j} = \frac{\boldsymbol{\sigma}_{x,j}}{2\eta_{x,j}(\bar{\tau}_x, p, S_x, T)} \tag{20}$$

where $\eta_{x,j}$ is the viscosity in the dashpot of Maxwell element j and relaxation process x. It is a function of the equivalent stress $\bar{\tau}_x$, the hydrostatic stress $p = -\mathrm{tr}(\boldsymbol{\sigma})/3$, the state parameter S_x and the absolute temperature T:

$$\eta_{x,j} = \eta_{0x,j} \frac{\bar{\tau}_x/\tau_{0x}}{\sinh(\bar{\tau}_x/\tau_{0x})} \exp\left(\frac{\mu_x p}{\tau_{0x}}\right) \exp(S_x) \exp\left[\frac{\Delta H_x}{R}\left(\frac{1}{T} - \frac{1}{T_{\mathrm{ref}}}\right)\right] \tag{21}$$

In this equation $\eta_{0x,j}$ is the initial viscosity, τ_{0x} is the characteristic shear stress, μ_x is the pressure dependency parameter, ΔH_x is the activation enthalpy, R is the gas constant, and $T_{\mathrm{ref}} = 298.15$ K is the reference absolute temperature. The equivalent stress is defined as:

$$\bar{\tau}_x = \sqrt{\frac{1}{2}\boldsymbol{\sigma}_x : \boldsymbol{\sigma}_x} \tag{22}$$

with $\boldsymbol{\sigma}_x = \sum \boldsymbol{\sigma}_{x,j}$, whereas the definition of the characteristic shear stress is:

$$\bar{\tau}_{0x} = \frac{k_{\mathrm{B}} T}{V_x} \tag{23}$$

in which k_{B} is the Boltzmann constant, and V_x is the activation volume.

The state parameter S_x takes into account the thermodynamical history of the material, which in turn depends on its processing history. In the EGP model it is represented as a product of the aging parameter S_{ax} and the softening function $R_{\gamma x}$, i.e., $S_x = S_{\mathrm{ax}} R_{\gamma x}$. Since the influence of processing on the mechanical properties is not addressed in this study, the aging parameter is set to zero. Furthermore, the experimental results considered in this study show no flattening of the creep curves, which, if present, would indicate progressive aging.

The EGP model parameters are shown in Table 2, while the relaxation spectrum is listed in Table 3. As claimed in [18], a different crystallinity of PEEK in the composite material and that of neat PEEK may imply a different mechanical behavior of the polymer matrix. Hence, the calibration of the EGP parameters was done directly on the creep experiments of UD tapes. Because the extensometer was not used in the experiments, the relaxation spectrum implicitly takes into account the compliance effect of the machine grips, see Fig. 1. More accurate measurements of the strain response would result in re-calibration of the EGP and the cohesive law parameters.

The equivalent plastic strain $\bar{\gamma}_{\mathrm{p}}$ in the EGP model is computed by integrating the evolution law:

$$\dot{\bar{\gamma}}_{\mathrm{p}} = \frac{\bar{\tau}_{\alpha,1}}{\eta_{\alpha,1}}, \quad \bar{\tau}_{\alpha,1} = \sqrt{\frac{1}{2}\boldsymbol{\sigma}_{\alpha,1} : \boldsymbol{\sigma}_{\alpha,1}} \tag{24}$$

where $\bar{\tau}_{\alpha,1}$ is the equivalent stress associated with the mode of highest viscosity $\eta_{\alpha,1}$.

4.2. Transversely isotropic constitutive model for carbon fibers

With the assumption that failure processes take place only in the polymer matrix, carbon fibers are modeled with a hyperelastic transversely isotropic material model [30], with a small modification as presented in [17]. In the model, the Cauchy stress is decomposed in two parts:

$$\boldsymbol{\sigma} = \boldsymbol{\sigma}_{\mathrm{iso}} + \boldsymbol{\sigma}_{\mathrm{tri}} \tag{25}$$

where the neo-Hookean model [23] describes the isotropic stress tensor:

$$\boldsymbol{\sigma}_{\mathrm{iso}} = \frac{\mu}{J_i}(\mathbf{B} - \mathbf{I}) + \frac{\lambda}{J_i}\ln(J_i)\mathbf{I} \tag{26}$$

while the transversely isotropic part of the stress tensor is derived as:

$$\boldsymbol{\sigma}_{\mathrm{tri}} = J_i^{-1}\{2\beta(I_4-1)\mathbf{B} + 2[\alpha+\beta(I_1-3)+2\gamma(I_4-1)]\boldsymbol{a}\otimes\boldsymbol{a} - \alpha(\mathbf{B}\boldsymbol{a}\otimes\boldsymbol{a} + \boldsymbol{a}\otimes\mathbf{B}\boldsymbol{a})\} \tag{27}$$

In Eqs. (26) and (27) J_i is the determinant of the deformation gradient at an integration point, $\mathbf{B}$ is the left Cauchy–Green deformation tensor, $\mathbf{I}$ is the second-order unit tensor, $\boldsymbol{a}$ is the vector defining the material preferential stiffness direction in the deformed configuration. The invariants I_1 and I_4 are defined as:

$$\begin{aligned} I_1 &= \mathrm{tr}(\mathbf{B}) \\ I_4 &= \boldsymbol{a} \cdot \boldsymbol{a} \end{aligned} \tag{28}$$

The other model parameters assume the form as presented in [17]:

$$\begin{aligned} n &= \frac{E_1}{E_2} \\ m &= 1 - \nu_{23} - 2n\nu_{12}^2 \\ \lambda &= \frac{E_2(\nu_{23} + n\nu_{12}^2)}{m(1+\nu_{23})} \\ \mu &= \frac{E_2}{2(1+\nu_{23})} \\ \alpha &= \mu - G_{12} \\ \beta &= \frac{E_2(\nu_{12} + \nu_{23}\nu_{12} - \nu_{23} - n\nu_{12}^2)}{4m(1+\nu_{23})} \\ \gamma &= \frac{E_1(1-\nu_{23})}{8m} - \frac{\lambda+2\mu}{8} + \frac{\alpha}{2} - \beta \end{aligned} \tag{29}$$

The five elastic constants of the material model are shown in Table 4, where E_1 is the Young's modulus in the preferential stiffness direction. It was determined from quasi-static experiments on UD tapes under 0° off-axis angle. E_2 and ν_{23} are the Young's modulus and the Poisson's ratio defining the model behavior in the plane of isotropy, adopted according to [31]. G_{12} and ν_{12} are the shear modulus and the Poisson's ratio in the plane perpendicular to the isotropic plane. The former is determined in the process of fitting the experimental creep response of the composite material for 45° loading angle, while the latter is adopted according to [17], which ensures the computational stability of the hyperelastic constitutive model.

Table 3
Relaxation spectrum of the EGP model.

x,j	$G_{x,j}$ [MPa]	$\eta_{0x,j}$ [MPa s]
$\alpha,1$	521.96	$1.992 \cdot 10^{26}$
$\beta,1$	455.96	$4.965 \cdot 10^{22}$
$\beta,2$	385.58	$5.518 \cdot 10^{21}$
$\beta,3$	312.50	$6.761 \cdot 10^{20}$
$\beta,4$	238.85	$2.108 \cdot 10^{19}$
$\beta,5$	166.87	$1.591 \cdot 10^{15}$
$\beta,6$	98.51	$2.571 \cdot 10^{12}$
$\beta,7$	35.14	$7.086 \cdot 10^{9}$

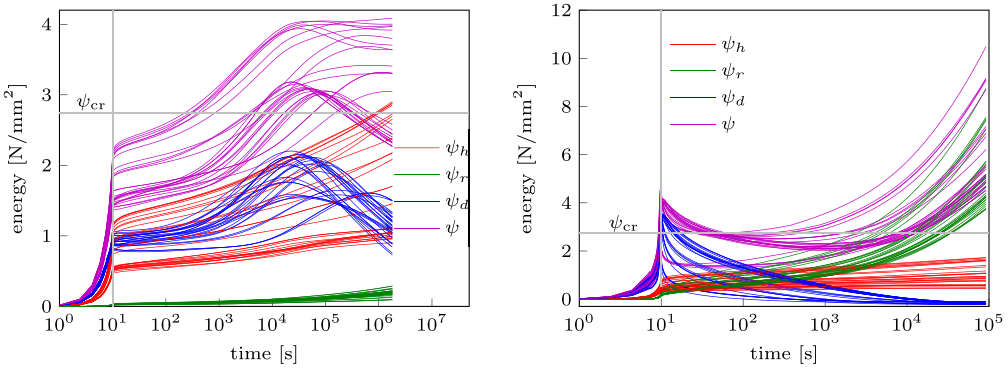

Fig. 5. Evolution of the Helmholtz free energy and its components in the EGP model for $\chi = 90°$ and $\sigma_{yy}^{\rm eng} = 95$ MPa (left), $\chi = 45°$ and $\sigma_{yy}^{\rm eng} = 112$ MPa (right); $T = 25$ °C.

Table 4
Elastic constants of the transversely isotropic constitutive model.

E_1 [GPa]	E_2 [GPa]	G_{12} [GPa]	ν_{12}	ν_{23}
125	15	5	0.05	0.3

4.3. Microcrack initiation

The EGP model can capture creep deformation but it does not predict creep rupture in the material. According to Fig. 4, as creep deformation proceeds, there is stress relaxation in the Maxwell elements, which is picked up by the elastic hardening and hydrostatic stress components. In the limit of complete stress redistribution the creep deformation would reach a constant value without failure taking place.

In order to simulate the creep rupture mechanism in the RVE the cohesive zone modeling is applied. When a suitable initiation criterion is satisfied, a cohesive segment is inserted between two bulk finite elements on the fly [32]. A stress-based initiation criterion seems not suitable for capturing creep rupture because the microscale stresses might remain less than a prescribed critical value, while rupture may still occur if the creep load is kept long enough, making it difficult to actually define the critical stress. Therefore, we also account for the deformation component by proposing an initiation criterion that is energy-based. According to the Reiner–Weissenberg theory [19], material fails when the deviatoric part of the stored energy attains a critical value. In a slightly modified form this theory was followed by Brüller [33] to model failure in thermoplastic polymers, and by Hiel et al. [34] to model failure of polymer composites. Instead of the deviatoric part, as stated by Brinson [1], the total stored energy may be a better indicator of failure in composites. Following this idea, we propose that a cohesive microcrack initiates when the total free energy reaches a critical value. In order to define the critical value $\psi_{\rm cr}$, it is pertinent to plot the evolution of the free energy and its components for different loading angles, without adding cohesive segments in the micromodel. For several points in the RVE that exceed the eventually determined critical energy this evolution is shown in Fig. 5, for two loading angles, 90° and 45°, and two stress levels, 95 MPa and 112 MPa, respectively. Vertical and horizontal gray lines show the time instance on which the constant stress level is reached and the eventual calibrated value for the critical energy value, respectively. The total free energy evolves differently for the two loading angles, resulting in much lower energy values for $\chi = 90°$. Much of the difference is due to the significantly different change in the hardening part of the free energy, which for $\chi = 45°$ attains a high value. The homogenized strain evolution corresponding to these two loading cases is shown in Fig. A.23 in the Appendix.

The chosen value for the critical energy is $\psi_{\rm cr} = 2.74$ N/mm^2. This value needs to be low enough to have progressive failure in $\chi = 90°$ simulations, but high enough to avoid premature failure in $\chi = 45°$ simulations. The balancing between these two requirements is due to the large difference in the stored energy for the two loading angles. The critical value intersects the total energy already in the phase of increasing loading ($t < 10$ s) for the 45° loading angle. In this phase the driving energy part reaches a maximum after which relaxation takes place and this energy part reduces, for some points even to a negative value, see Fig. 5(right). What causes the unexpected negative energy deserves special attention in future investigations, but is outside the scope of this paper. When computing the total free energy, which remains positive in a deformed state, the possible negative values of the driving energy are precluded by performing the Macaulay operation: $\langle \psi_{\rm d} \rangle = \max(0, \psi_{\rm d})$. Since this energy component corresponds with the Maxwell viscous element, we intend to enable the relaxation process in the early loading phase. Therefore, an auxiliary condition is added, whose role is to prevent early microcrack initiation and enable relaxation in the 45° loading case. The auxiliary condition states that the driving energy part must be less than a prescribed fraction of the total free energy for initiation to happen:

$$\frac{\langle \psi_{\rm d} \rangle}{\psi_{\rm h} + \psi_{\rm r} + \langle \psi_{\rm d} \rangle} < 0.73 \tag{30}$$

How the energy ratio in Eq. (30) changes with time for the off-axis angles of 90° and 45° is shown in Fig. 6, where the data correspond to the same points as in Fig. 5. For the 90° loading angle the reported results show no intersection between the energy ratio and the auxiliary condition. On the other hand, for the 45° loading angle the value of 0.73 crosses the energy ratio close to the end of increasing loading phase, practically preventing the microcrack initiation in the early loading phase.

With the energy-based initiation criterion, it is possible to have cohesive segments along every edge of the bulk finite element. Since this situation may lead to computational instability, initiation is allowed along maximum two edges of the 12-node wedge-shaped finite element, while the remaining edge must remain intact. Another consequence of the energy-based initiation criterion for interelement cohesive segments is that the orientation of the cohesive zone may be any orientation defined by the edges of the bulk finite element. To prevent initiation along a physically less favorable direction, a cohesive segment cannot initiate if the angle between the projection of the maximum principal stress direction in the xy-plane of the RVE (the plane perpendicular to fiber direction) and the potential cohesive surface normal is larger than 60°.

4.4. Time-dependent cohesive zone model

After initiation takes place, a cohesive zone model controls the process of decohesion. A CZ model used as the base model in this work is the shifted mixed-mode damage cohesive law elaborated by Liu et al. [35], and extended to 3D in [18]. Mode I representation of this

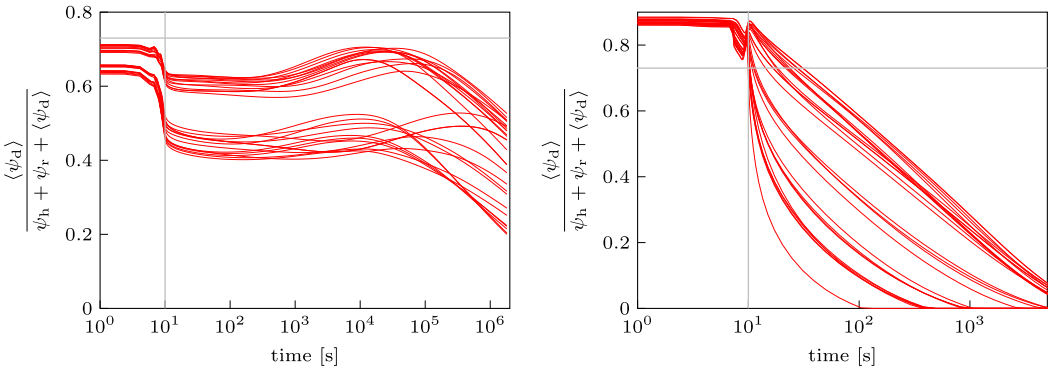

Fig. 6. Ratio of driving free energy component and the total free energy for $\chi = 90°$ and $\sigma_{yy}^{\text{eng}} = 95$ MPa (left), $\chi = 45°$ and $\sigma_{yy}^{\text{eng}} = 112$ MPa (right); $T = 25$ °C; horizontal gray line at 0.73 defines the energy ratio above which microcrack initiation is not allowed.

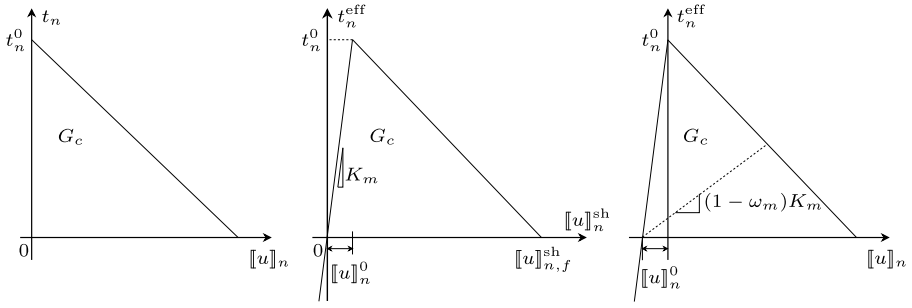

Fig. 7. Mode I representation of the shifted mixed-mode damage cohesive law.

CZ model is shown in Fig. 7, where the normal traction component is plotted versus the normal component of the displacement jump. The area below the diagram is defined as the fracture energy G_c. When cohesive segment is inserted in the RVE the traction on the cohesive surface is non-zero, while the displacement jump is zero. In a mixed-mode loading scenario this combination would lead to the singularity problem [24], therefore the cohesive law is evaluated with a shifted displacement jump:

$$[\![\bar{\mathbf{u}}]\!]^{\text{sh}} = [\![\bar{\mathbf{u}}]\!] + [\![\bar{\mathbf{u}}]\!]^0 \tag{31}$$

where $[\![\bar{\mathbf{u}}]\!]^0$ is the displacement shift:

$$[\![\bar{\mathbf{u}}]\!]^0 = \frac{\bar{\mathbf{t}}^0}{K_m} \tag{32}$$

Here, $\bar{\mathbf{t}}^0$ is the traction vector at the moment of CZ initiation, and K_m is the dummy stiffness. The constitutive law for the traction is given by the following relation:

$$\bar{\mathbf{t}} = (\mathbf{I} - \boldsymbol{\Omega}) K_m [\![\bar{\mathbf{u}}]\!]^{\text{sh}} = (\mathbf{I} - \boldsymbol{\Omega}) \bar{\mathbf{t}}^{\text{eff}} \tag{33}$$

In this equation $\bar{\mathbf{t}}^{\text{eff}}$ is the effective traction on the cohesive surface, $\mathbf{I}$ is the second-order unit tensor, and $\boldsymbol{\Omega}$ is the damage tensor accounting for stiffness recovery in normal direction under compression:

$$\Omega_{ij} = \omega_m \delta_{ij} \left(1 + \delta_{i1} \frac{\langle -t_n^{\text{eff}} \rangle}{t_n^{\text{eff}}} \right) \tag{34}$$

The $\boldsymbol{\Omega}$ depends on the damage variable ω_m which is a non-decreasing function of time defined as:

$$\omega_m = \max_{\tau \le t} \begin{cases} 0, & \Delta \le \Delta_0 \\ \frac{\Delta_f}{\Delta} \left(\frac{\Delta - \Delta_0}{\Delta_f - \Delta_0} \right), & \Delta_0 < \Delta < \Delta_f \\ 1, & \Delta > \Delta_f \end{cases} \tag{35}$$

where Δ is the equivalent shifted displacement jump:

$$\Delta = \left[\langle\langle [\![u]\!]_n^{\text{sh}} \rangle\rangle^2 + ([\![u]\!]_s^{\text{sh}})^2 + ([\![u]\!]_t^{\text{sh}})^2 \right]^{1/2} \tag{36}$$

with the subscripts n, s and t representing normal and two shear orthonormal directions respectively. In Eq. (35) Δ_0 is the equivalent displacement jump at the instant of initiation:

$$\Delta_0 = \frac{t_{\text{eq}}^0}{K_m} \tag{37}$$

which depends on the equivalent traction t_{eq}^0 at the same moment:

$$t_{\text{eq}}^0 = \left[(t_n^0)^2 + (t_s^0)^2 + (t_t^0)^2 \right]^{1/2} \tag{38}$$

The decohesion process is completed when the equivalent shifted displacement jump attains a failure value Δ_f:

$$\Delta_f = \frac{2G_c}{t_{\text{eq}}^0} \tag{39}$$

The fracture energy G_c provided to the model interpolates between a lower bound value G_{Ic} and an upper bound value G_{IIc} as a function of the local stress ratio at the moment of CZ initiation [18], see Fig. 8. In this figure $t_\perp$ is the stress component on the cohesive surface perpendicular to the fiber direction when the cohesive segment initiates, while $t_\parallel$ is the stress component parallel with the fiber direction.

This CZ model is time-independent, and in a creep rupture scenario the traction vector on the cohesive surface may not change at all as the time progresses. This fact is explained with a simple example illustrated in Fig. 9. A polymer material is loaded in tension with a constant stress. As the consequence of the creep stress a cohesive segment is inserted in the polymer material when a suitable initiation criterion is satisfied. Due to the equilibrium condition the stress transmitted through the CZ from the right piece of the material to the left piece is equal to the creep stress applied. Given the viscous material, the deformation will keep increasing, but for the same amount for the left and the right part, keeping the displacement jump unchanged from the previous time instants. Being purely a function of the displacement jump, the cohesive law would keep the constant stress in this deformation process, and rupture would never occur. This fact holds true for any CZ model whose traction vector is defined only in terms of the displacement jump.

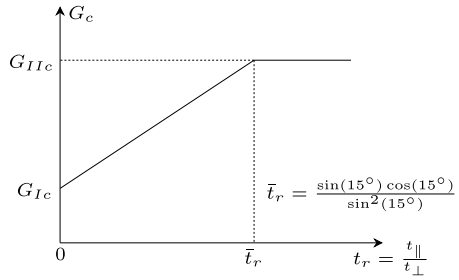

Fig. 8. Cohesive law fracture energy depending on local stress ratio when cohesive segment is initiated.

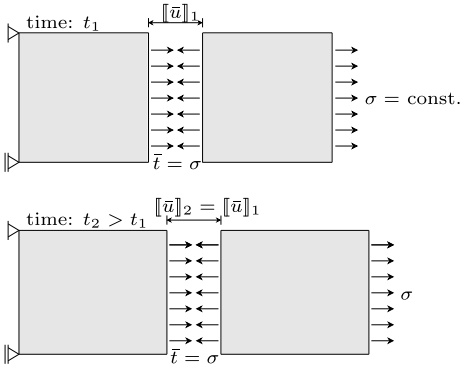

Fig. 9. Displacement jump and traction of a cohesive zone governed by time-independent constitutive model during creep loading of polymer material not changing at different time instants.

The time-independent cohesive law remains ineffective also in the context of a more complex RVE geometry. Some decohesion due to stress redistribution is possible, but any changes in traction are very slow resulting in the material time-to-failure being much longer than experimentally observed. Due to this reason a modification is proposed to the base cohesive law, such that the traction on the cohesive surface also depends on time through the viscous degradation tensor $\mathbf{D}_v$:

$$\bar{\mathbf{t}} = (\mathbf{I} - \boldsymbol{\Omega})\mathbf{D}_v K_m [\![\bar{\mathbf{u}}]\!]^{\text{sh}} \tag{40}$$

To define components of the tensor $\mathbf{D}_v$, the viscous degradation variable D_v at time step n is defined as a non-increasing function:

$$D_v^n = D_v^{n-1} \exp(-\Delta t/\tau_{\text{r}}) \tag{41}$$

where Δt is the time increment, and τ_{r} is the relaxation time which depends on the normal component of the traction vector through the following relation:

$$\tau_{\text{r}} = \tau_{\text{r0}} \frac{t_n/(D_v t_0)}{\sinh[t_n/(D_v t_0)]} \tag{42}$$

In this equation $\tau_{\text{r0}}(T)$ is the initial relaxation time that depends on the temperature, while $t_0(T)$ is the traction-like variable also dependent on the temperature. This constitutive relation for the relaxation time is chosen on the basis of experimentally observed rupture time, see Fig. 10, which indicates that a small change in the applied stress causes a significant change in the rupture time. The shift function $[t_n/(D_v t_0)]/\sinh[t_n/(D_v t_0)]$ has a similar counterpart in the viscosity definition of the EGP model, Eq. (21), and its role is to shift the initial relaxation time given an adequate stress measure. In this regard, the time-dependent component of the cohesive law can be perceived as an Eyring-based. It should be noted that τ_{r} moves towards the initial value τ_{r0} as t_n decreases. Finally, inclusion of D_v in Eq. (42) prevents the evolution in the relaxation time from drastically slowing down the rupture event, after the minimum creep strain-rate is observed.

Table 5
Model parameters of time-dependent cohesive law.

K_m [N/mm^3]	G_{Ic} [N/mm]	G_{IIc} [N/mm]	τ_{r0}(25 °C) [s]	t_0(25 °C) [N/mm^2]
10^7	0.03	0.095	10^9	4.6

It can be shown that for constant τ_{r} the discrete evolution law in Eq. (41) is equivalent to the following continuous rate equation:

$$\dot{D}_v = -\frac{D_v}{\tau_{\text{r}}} \tag{43}$$

Under the assumption that τ_{r} is changing more slowly than D_v, Eq. (41) provides a more accurate time-integration of this rate equation than the direct Euler forward approach.

The viscous degradation tensor has three non-zero components corresponding with the orthogonal directions defining the orientation of the cohesive surface:

$$\mathbf{D}_v = \begin{bmatrix} D_n & & \\ & D_s & \\ & & D_t \end{bmatrix} \tag{44}$$

With the scalar D_v defined in Eq. (41), the components of the tensor $\mathbf{D}_v$ assume the following form: $D_s = D_t = D_v$, whereas the component D_n restores the initial stiffness in the normal direction, in the case of compression:

$$D_n = \begin{cases} D_v, & t_n \geq 0 \\ 1, & t_n < 0 \end{cases} \tag{45}$$

The initial value of D_v is equal to 1, and evolves towards 0 with time. To simplify the linearization and implementation of the cohesive law, the normal traction component and the viscous degradation variable from the previous converged time step are used in Eq. (42).

The time-dependent components of the cohesive law trigger a decrease in the traction due to creep loading and subsequently a change in the displacement jump. One possible trajectory of the normal traction component plotted against the normal jump component is depicted in Fig. 11. As a consequence of the stress relaxation, the actual fracture energy is lower than G_c defined for the time-independent cohesive law. The parameters used to run simulations with the described time-dependent cohesive law are listed in Table 5.

5. Results and discussion

In this section several examples are considered to illustrate the model performance. Since the main purpose of the paper is to formulate the framework and indicate necessary components to model creep deformation and rupture, only one RVE was considered in the study, with 9 (3 × 3) fibers in total and the fiber diameter of 5 μm.

The first example aims at showing the inability to model creep rupture with the time-independent cohesive zone model, i.e., without the viscous degradation introduced in Eq. (40). In Fig. 12 the homogenized strain-rate is plotted versus time for two off-axis angles, 45° and 90°, and several stress levels. The strain-rate at the current time step is computed as: $\dot{\varepsilon}_{yy}^n = (\varepsilon_{yy}^n - \varepsilon_{yy}^{n-1})/\Delta t$, where ε_{yy}^n is obtained from Eq. (7) or Eq. (9). Unless otherwise stated, the creep stress is reached at $t = 10$ s. After the increasing loading phase is completed, the strain-rate corresponding to the creep stress is gradually decreasing. When the initiation criterion is satisfied cohesive segments are inserted in the RVE, causing a disturbance in the displacement field, which is reflected in oscillations of the homogenized strain-rate. Apart from these brief oscillations, the strain-rate is monotonically decreasing and comparison with experiments in terms of the rupture time cannot be made.

Next, the difference when considering a constant engineering stress and a constant true stress in the analysis is illustrated in Fig. 13. Without inserting cohesive segments in the RVE, the engineering strain

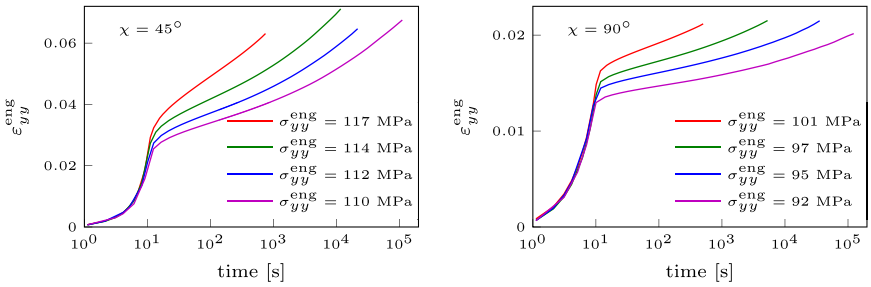

Fig. 10. Experimentally measured engineering strain versus time due to constant engineering stress for two loading angles; constant load level is reached after 10 s; failure of specimen coincides with termination of the strain curves.

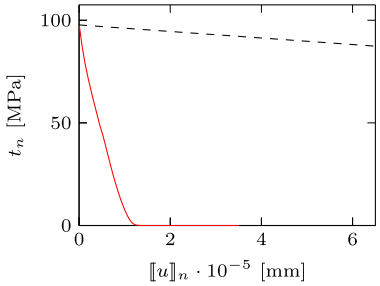

Fig. 11. Red line representing one possible trajectory of the normal traction component as function of the displacement jump; actual fracture energy of time-dependent cohesive law is reduced due to viscous degradation; dashed line represents quasi-static cohesive law.

is computed for two loading angles, and comparison is also made with experimental data. For the homogenized strain of approximately 0.03 and higher, the difference in the outcome for the two stress measures becomes significant. A constant engineering stress in tension implies an increase in the actual stress on the material, see Eq. (8), leading to higher strains as opposed to the case of a constant true stress applied. Because the experimental results are reported in terms of the engineering strain as the result of a constant engineering stress, the following simulation results consider engineering stress and strain measures.

The ability of the time-dependent cohesive law to trigger a global increase in the homogenized creep strain-rate is shown in Fig. 14(right), where the strain-rate evolution corresponding to $\chi = 90°$, $T = 25$ °C and different stress levels is plotted. The minimum point in the strain-rate curve is taken as the point of rupture and used to define the material time-to-failure. Comparison of the homogenized strain plotted against time with experimental results is shown in Fig. 14(left), where the rupture points obtained from the strain-rate plot are also indicated. The model predicts reasonably well the creep strain response, whereas the accuracy in predicting the rupture time decreases with a decrease in the creep stress. The largest difference is for the stress $\sigma_{yy}^{\mathrm{eng}} = 92$ MPa. It is important to notice that in all considered cases the experimentally observed failure mechanism is brittle, with the lack of tertiary creep and without large macroscopic deformation. For plotting the strain-rate curves in Fig. 14 and the subsequent figures for $T = 25$ °C, median filtering is performed on the data, see [36]. This is because the oscillations become substantial around the minimum point, making it difficult to clearly mark the rupture point. Comparison of the filtered curves with the unfiltered ones is shown in Fig. B.24.

In the next example the off-axis angle of 45° is considered, with the temperature $T = 25$ °C and different stress levels. In Fig. 15 the homogenized strain and the homogenized strain-rate are plotted versus time. Similarly to the previous example, the creep strain response is reasonably well reproduced by the model as well as the general trend of a rupture time that decreases with increasing stress. The difference in the predicted rupture time relative to the experiment is pronounced for the stress level of 110 MPa and 117 MPa.

The possibility to model the creep response at an elevated temperature is presented next. First, all the parameters are kept the same as in the previous cases, including the initial relaxation time τ_{r0} and the traction-like variable t_0 in Eq. (42) The evolution of the homogenized strain and strain-rate are shown in Fig. 16, for $\chi = 90°$, $T = 90$ °C and different stress levels. The creep strain is captured reasonably well, except for $\sigma_{yy} = 72$ MPa. According to the experimental observation there is a significant change in the response when increasing the creep stress from 71 MPa to 72 MPa. This change is not captured by the model. Correspondingly, the model overestimates the time-to-failure that is experimentally observed (a minimum in strain-rate is not observed in the considered time range, see Fig. 16). On the other hand, if different values are assigned to τ_{r0} and t_0 at the higher temperature, better results are obtained. Accordingly, we consider a case with $\tau_{\mathrm{r0}}(90\ °\mathrm{C}) = 10^3$ s and $t_0(90\ °\mathrm{C}) = 10.5\ \mathrm{N/mm^2}$, see Fig. 17, where the homogenized strain and strain-rate are plotted versus time. The newly obtained results lead to a better match with the experiment in terms of the rupture time, even though a difference remains present, particularly for a creep stress of 72 MPa.

Although the homogenized strain and strain-rate curves are plotted in the previous graphs, the numerical framework also provides for the microstructural distribution of stress, strain and history variables. As an example, the distribution of the equivalent plastic strain is shown in Fig. 18 for different off-axis angles, temperatures and stress levels, at the moment of failure $t = t_{\mathrm{f}}$ and at the time when the constant stress level is reached, $t = 10$ s, for one of the cases. As can be observed from the figure, after $t = 10$ s there is practically no visible plastic strain in the model. The situation has changed at the moment of rupture, with significant plastic strain predicted in the polymer matrix throughout the RVE domain. Notably, the case of $\chi = 90°$ and $T = 25$ °C features much less plastic strain than the other depicted cases, which is due to the higher viscosity compared to the $T = 90$ °C case, see Eq. (21), and the lower deviatoric deformation compared to the $\chi = 45°$ case.

Beside the equivalent plastic strain, it is interesting to show initiated cohesive zones when the minimum creep strain-rate is reached, that defines the rupture time and is followed by a sudden change in the homogenized strain. In Fig. 19 cohesive segments in the RVE at $t = t_f$ are shown for two loading angles and two temperature conditions. The number of initiated cohesive segments varies with the loading angle and temperature. For $T = 90$ °C this number is rather limited, indicating that a small zone of degrading material triggers a sudden change in the creep strain and leads to rupture. The effect of cohesive segments on the evolution of homogenized strain is illustrated in Fig. 20, for the same loading cases considered in the previous figure. Again it is observed that localization of deformation in the present framework cannot be achieved without a cohesive zone model.

The microscale model accounts for finite strains in the material, which implies the change in orientation of the RVE with respect to the loading direction, see Fig. 2. It was already shown that this rotation of the RVE has an important effect on the material strength for a

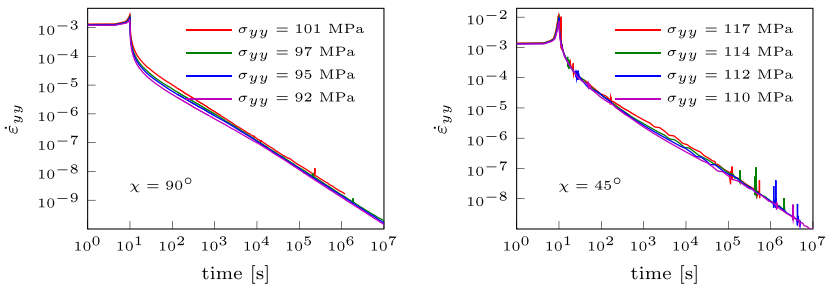

Fig. 12. Homogenized strain-rate versus time for $T = 25$ °C, different off-axis angles and stress levels, with time-independent cohesive law governing decohesion process.

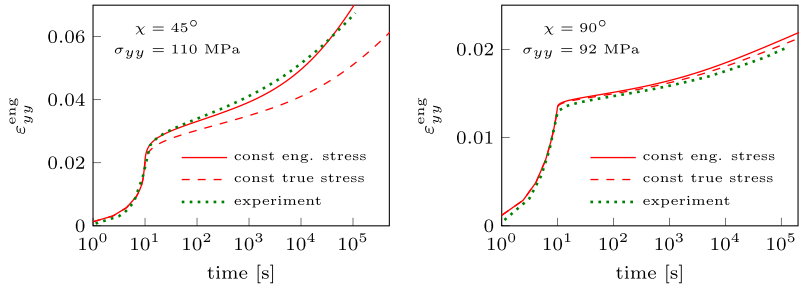

Fig. 13. Comparison of experimental results with simulations assuming constant engineering stress and constant true stress on the material, for two off-axis angles and $T = 25$ °C.

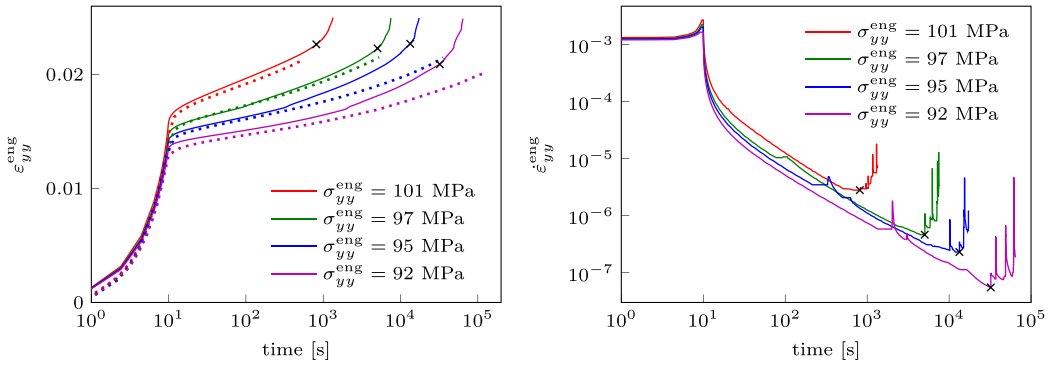

Fig. 14. Evolution of homogenized strain for $\chi = 90°$ and $T = 25$ °C (left); evolution of homogenized strain-rate (right); solid lines: model response, markers: model creep rupture points, dotted lines: experiment.

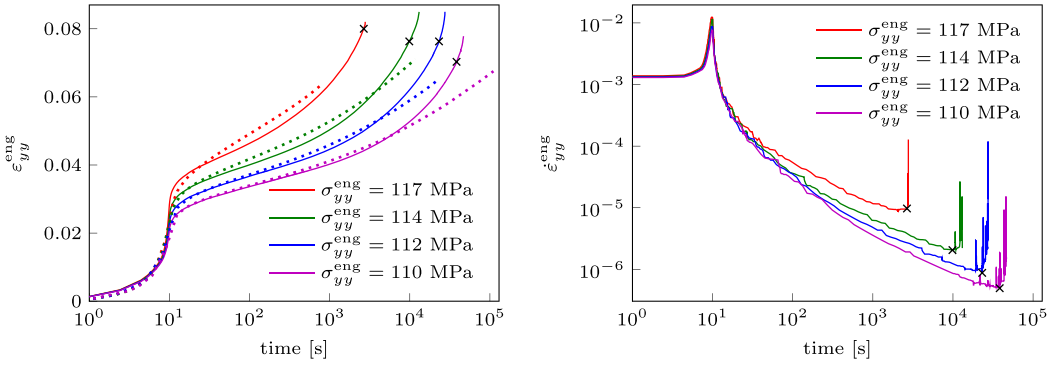

Fig. 15. Evolution of homogenized strain for $\chi = 45°$ and $T = 25$ °C (left); change in homogenized strain-rate with time (right); solid lines: model response, markers: model creep rupture points, dotted lines: experiment.

constant strain-rate loading scenario [18]. The effect of this rotation on the creep response is illustrated next. In Fig. 21 the RVE response, without including the rupture process, is plotted for when the rotation is allowed ($\phi \neq 0$) as well as for when the rotation is restrained ($\phi = 0$) in comparison with the experiment. This is done for three loading angles: 15°, 30° and 45°. The change in orientation implies an alignment of the stiff fibers with the loading direction and the change in the actual off-axis angle, which reduces the material compliance. The rotation of the microstructure has a drastic effect on the creep response for lower off-axis angles: 15° and 30°. For these loading angles the fibers carry most of the loading, and a small variation in the off-axis angle leads to a significant increase in the material stiffness,

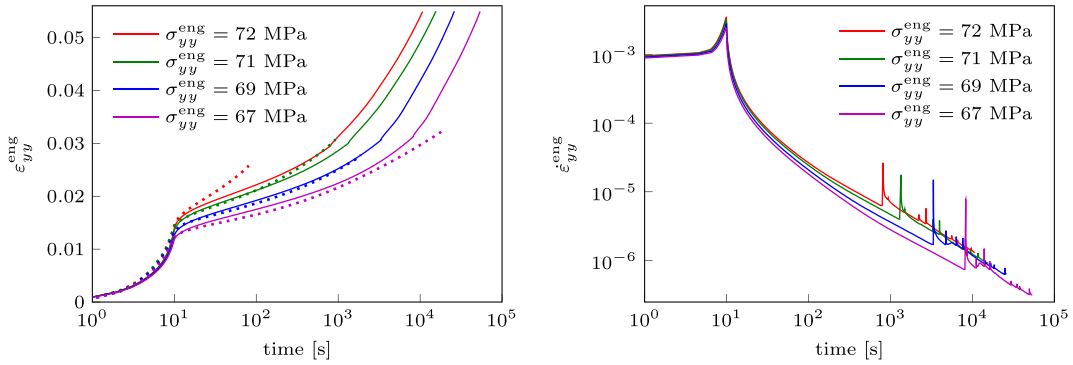

Fig. 16. Creep response at elevated temperature with all parameters the same as before; homogenized strain versus time for $\chi = 90°$ and $T = 90$ °C (left); evolution of homogenized strain-rate (right); solid lines: model response, dotted lines: experiment.

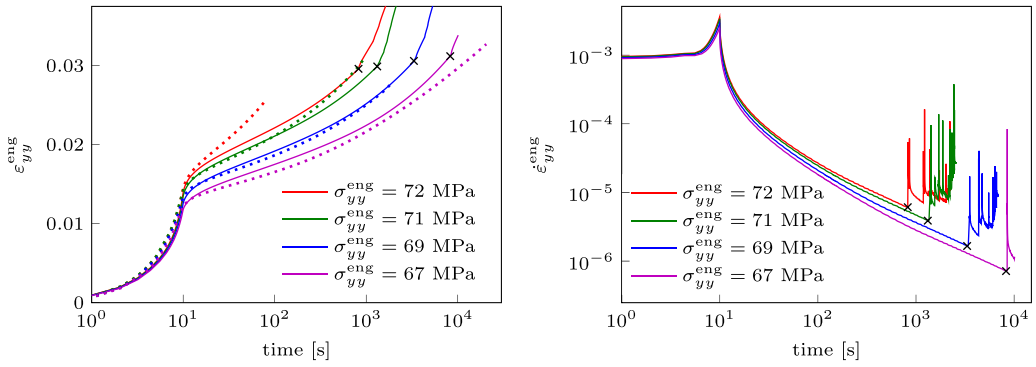

Fig. 17. Creep response at elevated temperature with updated parameters for the time-dependent part of the cohesive model: $\tau_{r0}(90\ °\text{C}) = 10^3$ s, and $t_0(90\ °\text{C}) = 10.5$ N/mm^2; evolution of homogenized strain for $\chi = 90°$, $T = 90$ °C (left); homogenized strain-rate versus time (right); solid lines: model response, markers: model creep rupture points, dotted lines: experiment.

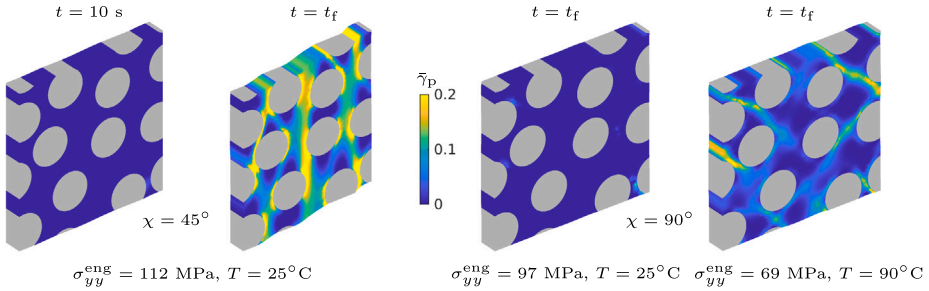

Fig. 18. Distribution of equivalent plastic strain in RVE at the end of increasing loading phase $t = 10$ s, and when failure is observed $t = t_f$ for different off-axis angles, stress levels and temperatures.

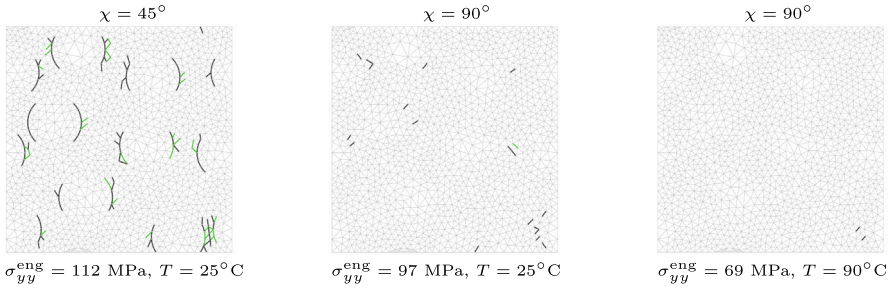

Fig. 19. Black lines representing degrading cohesive elements at the moment of minimum creep strain-rate in the RVE, which coincides with defined rupture time; green lines indicate unloading cohesive segments, whereas gray lines represent finite element mesh.

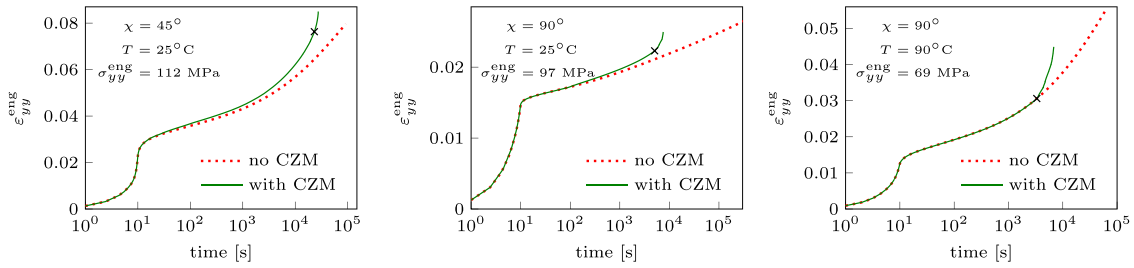

Fig. 20. Evolution of homogenized strain without cohesive zone model (CZM), and with cohesive zone model in the RVE, for different loading angles and temperature conditions; x marks predicted rupture time.

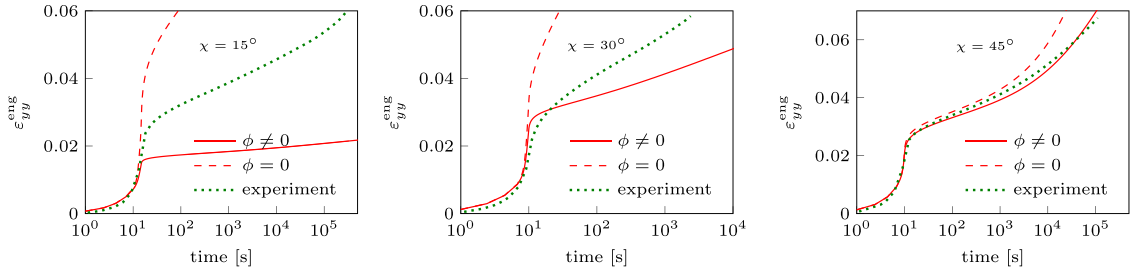

Fig. 21. Creep response of rotating RVE ($\phi \neq 0$) and non-rotating RVE ($\phi = 0$) compared with experiments for $T = 25$ °C and three off-axis angles: 15° (290 MPa), 30° (154 MPa) and 45° (110 MPa); creep stress for $\chi = 15°$ reached at $t = 15$ s.

with a corresponding decrease of the creep deformation rate. Given the experimental setup which does not allow for completely free shear deformation as assumed in the rotating RVE simulation (cf. Fig. 2), it may be expected that the experimental response is a combination of the two limit cases considered here: one in which material points align with the loading direction and the other in which orientation of material points is fixed. This hypothesis may be checked by a multiscale analysis, in which different integration points represented by individual RVEs would undergo different deformation depending on their position in the specimen. The stiffening effect due to the reorientation of the microstructure is present for $\chi = 45°$ as well, although to a lesser extent. It is because of this reason that the creep rupture time was compared with the experiments for $\chi = 45°$, and also $\chi = 90°$ for which there is no rotation of the microstructure during the loading process.

A recommendation stemming from the previous discussion is that numerical models aiming to simulate the mechanical behavior of orthotropic materials should account for the potential reorientation of the microstructure in the course of deformation. Quite often semi-analytical models to predict the creep behavior of composites under off-axis loading assume an equation which, among other parameters, depends on an off-axis angle. In the prediction, this angle is assumed a constant. Raghavan and Meshii [37] have proposed one such model to predict creep response of UD composites. For the off-axis angle of 30° and 60° they report more compliant results than experimentally obtained. Beside the explanation provided therein, an additional reason for this discrepancy might be a change in the actual off-axis angle during the process of creep deformation.

Bauwens-Crowet et al. [38] noticed a relation between the response of glassy polymers when tested under constant strain-rate and creep loading conditions. Namely, when plotted in a semi-log plot, yield stresses versus the corresponding constant strain-rates and creep stresses versus the corresponding minimum creep strain-rates lie on a single straight line. Erartsin et al. [4] confirmed the similar relation for UD glass/iPP composites for different off-axis angles, only instead of the yield stress, the failure stress of the composite material is paired with the strain-rate. Fig. 22 shows the plot for the material system

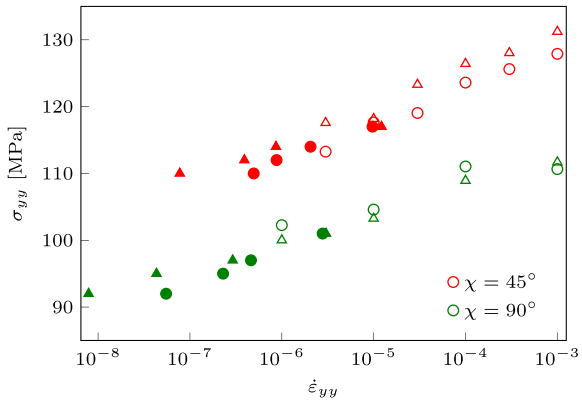

Fig. 22. Material failure stress versus corresponding strain-rate, obtained from the model (circles) and from the experiment (triangles); empty markers represent data for constant strain-rate loading case [18], filled markers represent creep data.

investigated here, with creep results (filled markers) from this paper together with constant strain-rate results from [18] (empty markers). Results from $\chi = 45°$ and $\chi = 90°$ are shown in red and green respectively, triangles are used for experimental measurements and circles for simulation results. As observed from the figure, the experimental creep data indeed follow the trend established by the constant strain-rate data. On the other hand, the trend is less followed by the creep data as predicted by the model, resulting in a lower stress dependency of the minimum creep strain-rate. The comparison of the numerical model presented in this paper with the model from [18] is made, even though notable differences exist between the two. The cohesive zone model used in [18] does not feature the viscous degradation term and assumes a different initiation criterion. Furthermore, the relaxation spectra of the EGP model are different. For the constant strain-rate simulations, a relaxation spectrum was calibrated on stress–strain curves obtained from extensometer measurements. Finally, the stress values computed

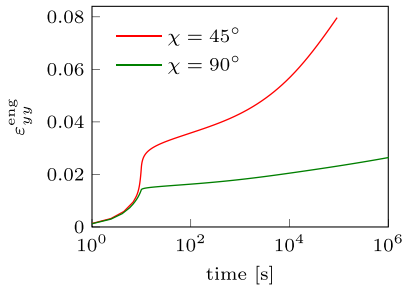

Fig. A.23. Homogenized strain evolution without initiated cohesive zones for two loading cases: 45° (112 MPa) and 90° (95 MPa); creep stress reached at $t = 10$ s.

in [18] are the Cauchy stress values, as opposed to constant engineering stress considered in creep simulations.

A unified numerical framework to model progressive failure of a UD composite material under off-axis creep, constant strain-rate and eventually under general time-dependent loading has not yet been achieved, but the formulations provided in this paper and our preceding one on constant strain-rate tests together introduce essential ingredients for this purpose.

6. Conclusion

In this paper a micromechanical model has been developed to simulate creep rupture in UD composites subjected to off-axis loading. The main ingredients of the model are a state of the art rate-dependent plasticity model, a recently developed formulation for off-axis loading on RVEs and a new time-dependent cohesive formulation. Creep deformation in the polymer matrix of the RVE is represented by the viscosity-dependent Eindhoven Glassy Polymer material model. The creep rupture process, which terminates creep deformation, is triggered by inserting cohesive segments along the finite element edges when an initiation criterion is satisfied. For this matter, an energy-based criterion depending on the critical Helmholtz free energy stored in the polymer matrix is proposed. After the CZ initiates, the necessity to apply a time-dependent cohesive law to further drive the decohesion process in creep loading is illustrated. The composite material eventually fails when the homogenized creep strain-rate of the RVE reaches a minimum value, which defines the creep rupture time.

The model is compared with original experiments on UD thermoplastic carbon/PEEK composite system tested at different stress levels, temperatures and loading angles. The accuracy in predicting creep deformation is satisfactory, but a discrepancy is observed in the rupture time. Three new parameters are introduced to describe creep rupture, the critical energy ψ_{cr} for initiation, the traction-like variable t_0 and the initial relaxation time of the cohesive law τ_{r0}. Of these, the last two needed to be made temperature-dependent to get a reasonable agreement with experimentally observed creep rupture times. Kinematical relations allow for finite strains and, correspondingly, the change in orientation of the RVE during the loading process. This reorientation affects the creep response, reducing the material compliance especially for lower off-axis angles.

CRediT authorship contribution statement

Dragan Kovačević: Writing – review & editing, Writing – original draft, Visualization, Software, Methodology, Investigation, Data curation, Conceptualization. **Bharath K. Sundararajan:** Writing – review & editing, Writing – original draft, Investigation, Data curation. **Frans P. van der Meer:** Writing – review & editing, Supervision, Software, Resources, Project administration, Methodology, Funding acquisition, Conceptualization.

Declaration of competing interest

The authors declare that they have no known competing financial interests or personal relationships that could have appeared to influence the work reported in this paper.

Data availability

Data presented in this article are available at the 4TU.ResearchData repository through http://dx.doi.org/10.4121/21835773.v1.

Acknowledgment

This research forms part of the research programme of DPI, project #811t17.

Appendix A

Homogenized strain curves for two loading cases ($\chi = 45°$ and $\chi = 90°$), without inserting cohesive segments are shown in Fig. A.23. The evolution of the creep deformation corresponds with the free energy evolution shown in Fig. 5.

Appendix B

The unfiltered strain-rate curves are compared with the filtered ones for RVE simulations with included cohesive segments and for two loading angles in Fig. B.24.

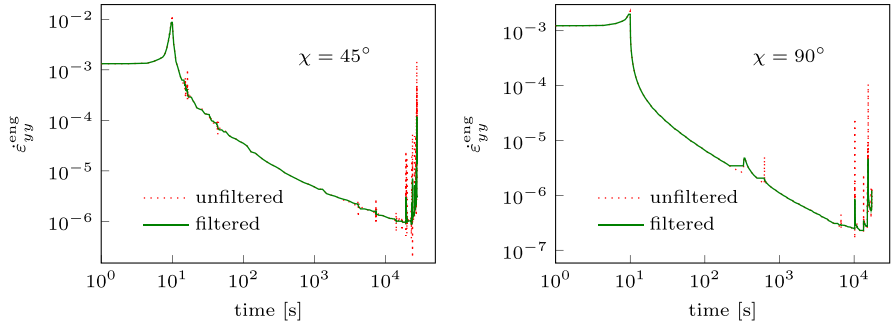

Fig. B.24. Unfiltered versus (median) filtered homogenized strain-rate curves for $\chi = 45°$ and $\sigma_{yy}^{\text{eng}} = 112$ MPa (left), and $\chi = 90°$ and $\sigma_{yy}^{\text{eng}} = 95$ MPa (right).

References

[1] Brinson HF. Matrix dominated time dependent failure predictions in polymer matrix composites. Compos Struct 1999;47(1–4):445–56.
[2] Eyring H. Viscosity, plasticity, and diffusion as examples of absolute reaction rates. J Chem Phys 1936;4(4):283–91.
[3] Kanters MJW, Kurokawa T, Govaert LE. Competition between plasticity-controlled and crack-growth controlled failure in static and cyclic fatigue of thermoplastic polymer systems. Polym Test 2016;50:101–10.
[4] Erartsin O, Amiri-Rad A, van Drongelen M, Govaert LE. Time-dependent failure of off-axis loaded unidirectional glass/iPP composites. J Appl Polym Sci 2022;139(23):52293.
[5] Spathis G, Kontou E. Creep failure time prediction of polymers and polymer composites. Compos Sci Technol 2012;72(9):959–64.
[6] Raghavan J, Meshii M. Prediction of creep rupture of unidirectional carbon fiber reinforced polymer composite. Mater Sci Eng A 1995;197(2):237–49.
[7] Schapery RA. On the characterization of nonlinear viscoelastic materials. Polym Eng Sci 1969;9(4):295–310.
[8] Lou YC, Schapery RA. Viscoelastic characterization of a nonlinear fiber-reinforced plastic. J Compos Mater 1971;5(2):208–34.
[9] Haj-Ali RM, Muliana AH. Numerical finite element formulation of the Schapery non-linear viscoelastic material model. Int J Numer Methods Eng 2004;59(1):25–45.
[10] Aboudi J. Micromechanical characterization of the non-linear viscoelastic behavior of resin matrix composites. Compos Sci Technol 1990;38(4):371–86.
[11] Haj-Ali RM, Muliana AH. A multi-scale constitutive formulation for the nonlinear viscoelastic analysis of laminated composite materials and structures. Int J Solids Struct 2004;41(13):3461–90.
[12] Jafaripour M, Taheri-Behrooz F. Creep behavior modeling of polymeric composites using Schapery model based on micro-macromechanical approaches. Eur J Mech A Solids 2020;81:103963.
[13] Gal E, Fish J. Anisotropic micromechanical creep damage model for composite materials: A reduced-order approach. Int J Multiscale Comput Eng 2008;6(2):113–21.
[14] Rabotnov YN. Creep rupture. In: Hetényi M, Vincenti WG, editors. Applied mechanics. International union of theoretical and applied mechanics, Berlin, Heidelberg: Springer; 1969, p. 342–9.
[15] Leckie FA, Hayhurst DR, Baker JF. Creep rupture of structures. Proc R Soc Lond Ser A Math Phys Eng Sci 1974;340(1622):323–47.
[16] Govaert LE, Schellens HJ, Thomassen HJM, Smit RJM, Terzoli L, Peijs T. A micromechanical approach to time-dependent failure in off-axis loaded polymer composites. Composites A 2001;32(12):1697–711.
[17] Kovačević D, van der Meer FP. Strain-rate based arclength model for nonlinear microscale analysis of unidirectional composites under off-axis loading. Int J Solids Struct 2022;250:111697.
[18] Kovačević D, Sundararajan BK, van der Meer FP. Microscale modeling of rate-dependent failure in thermoplastic composites under off-axis loading. Eng Fract Mech 2022;276:108884.
[19] Reiner M, Weissenberg K. A thermodynamic theory of the strength of the materials. Rheol Leaf 1939;10:12–20.
[20] Erartsin O, Van Drongelen M, Govaert LE. Identification of plasticity-controlled creep and fatigue failure mechanisms in transversely loaded unidirectional thermoplastic composites. J Compos Mater 2021;55(14):1947–65.
[21] van der Meer FP. Micromechanical validation of a mesomodel for plasticity in composites. Eur J Mech A Solids 2016;60:58–69.
[22] Ke L, Van der Meer FP. A computational homogenization framework with enhanced localization criterion for macroscopic cohesive failure in heterogeneous materials. J Theor Comput Appl Mech 2022.
[23] Belytschko T, Liu WK, Moran B, Elkhodary K. Nonlinear finite elements for continua and structures. John wiley & sons; 2014.
[24] van der Meer FP, Sluys LJ. A phantom node formulation with mixed mode cohesive law for splitting in laminates. Int J Fract 2009;158(2):107.
[25] Tervoort TA, Smit RJM, Brekelmans WAM, Govaert LE. A constitutive equation for the elasto-viscoplastic deformation of glassy polymers. Mech Time Depend Mater 1997;1(3):269–91.
[26] van Breemen LCA, Klompen ETJ, Govaert LE, Meijer HEH. Extending the EGP constitutive model for polymer glasses to multiple relaxation times. J Mech Phys Solids 2011;59(10):2191–207.
[27] Khaleghi H, Amiri-Rad A, Mashayekhi M. A thermodynamically consistent continuum damage model for time-dependent failure of thermoplastic polymers. Int J Plast 2022;154:103278.
[28] Coleman BD, Noll W. The thermodynamics of elastic materials with heat conduction and viscosity. Arch Rational Mech Anal 1963;13(1):167–78.
[29] Senden DJA, Krop S, van Dommelen JAW, Govaert LE. Rate- and temperature-dependent strain hardening of polycarbonate. J Polym Sci B Polym Phys 2012;50(24):1680–93.
[30] Bonet J, Burton AJ. A simple orthotropic, transversely isotropic hyperelastic constitutive equation for large strain computations. Comput Methods Appl Mech Engrg 1998;162(1):151–64.
[31] Miyagawa H, Sato C, Mase T, Drown E, Drzal LT, Ikegami K. Transverse elastic modulus of carbon fibers measured by Raman spectroscopy. Mater Sci Eng A 2005;412(1):88–92.
[32] Camacho GT, Ortiz M. Computational modelling of impact damage in brittle materials. Int J Solids Struct 1996;33(20):2899–938.
[33] Brüller OS. Energy-related failure criteria of thermoplastics: Energy-related failure criteria of thermoplastics. Polym Eng Sci 1981;21(3):145–50.
[34] Hiel CC, Brinson HF, Cardon AH. The nonlinear viscoelastic response of resin matrix composites. In: Marshall IH, editor. Composite structures 2. Dordrecht: Springer Netherlands; 1983, p. 271–81.
[35] Liu Y, van der Meer FP, Sluys LJ, Ke L. Modeling of dynamic mode I crack growth in glass fiber-reinforced polymer composites: Fracture energy and failure mechanism. Eng Fract Mech 2021;243:107522.
[36] Pratt WK. Digital image processing: PIKS Scientific inside, Vol. 4. Wiley Online Library; 2007.
[37] Raghavan J, Meshii M. Creep of polymer composites. Compos Sci Technol 1998;57(12):1673–88.
[38] Bauwens-Crowet C, Ots JM, Bauwens JC. The strain-rate and temperature dependence of yield of polycarbonate in tension, tensile creep and impact tests. J Mater Sci 1974;9(7):1197–201.